

Superconductivity from electronic interactions and spin-orbit enhancement in bilayer and trilayer graphene.

Alejandro Jimeno-Pozo,^{1,*} Héctor Sainz-Cruz,¹ Tommaso Cea,^{1,2} Pierre A. Pantaleón,¹ and Francisco Guinea^{1,3,4}

¹*Imdea Nanoscience, Faraday 9, 28049 Madrid, Spain*

²*Department of Physical and Chemical Sciences, University of L'Aquila, via Vetoio, Coppito, 67100 L'Aquila, Italy*

³*Donostia International Physics Center, Paseo Manuel de Lardizabal 4, 20018 San Sebastian, Spain*

⁴*Ikerbasque Foundation, Maria de Haro 3, 48013 Bilbao, Spain*

(Dated: 6th February 2023)

We discuss a Kohn-Luttinger-like mechanism for superconductivity in Bernal bilayer graphene and rhombohedral trilayer graphene. Working within the continuum model description, we find that the screened long-range Coulomb interaction alone gives rise to superconductivity with critical temperatures that agree with experiments. We observe that the order parameter changes sign between valleys, which implies that both materials are valley-singlet, spin-triplet superconductors. Adding Ising spin-orbit coupling leads to a significant enhancement in the critical temperature, also in line with experiment, and the superconducting order parameter shows locking between the spin and valley degrees of freedom.

Introduction. Recent experiments report cascades of correlated phases in Bernal bilayer graphene (BBG) [1–3]. One of them is spin-polarized superconductivity [1] with a critical temperature of $T_c \approx 26$ mK for fillings near the hole-doped van Hove singularity (vHs) when an out-of-plane electric field together with an in-plane magnetic field are applied on the system. Moreover, the authors of Ref. [4] have assembled a heterostructure in which a transition metal dichalcogenide (TMD) and BBG enter in synergy, making superconductivity appear over a broader range of electron filling and magnetic field, even without the latter, and enabling a striking increment in critical temperature to $T_c \approx 260$ mK, an effect that is attributed to Ising spin-orbit coupling (SOC). The stability and structural simplicity of BBG are clear advantages for experimental reproducibility, a major obstacle in Moiré materials [5], in which all samples differ due to angle disorder [6, 7] and strains [8]. A previous experiment showed that rhombohedral trilayer graphene (RTG) is a superconductor as well [9] and several theories about it have been proposed [10–20]. A key piece in the puzzle of graphene superconductors is that they all display cascades of flavour-symmetry-breaking phase transitions [1–3, 21–23], perhaps hinting at a common origin of superconductivity.

In these materials, and in BBG in particular, the proximity of superconductivity to flavour-polarized metallic phases and its Pauli limit violation point to an unconventional spin-triplet pairing mediated by electrons. In Ref. [24], a model is discussed in which short-range momentum-independent interactions and proximity to symmetry broken phases induce spin-triplet f -wave pairing. The authors of Ref. [25] propose a superconductivity from repulsion mechanism, in which the Coulomb interaction dressed by soft quantum-critical modes drives pairing. In their model, the magnetic field induces spin

imbalance, which makes the interaction acquire a dependence on frequency or on soft-mode momenta, leading to valley-singlet, spin-triplet s -wave or valley-triplet spin-triplet p -wave pairings, respectively. In Refs. [26, 27], a pairing mechanism mediated by acoustic phonons is investigated, which is compatible with spin-singlet s -wave and spin-triplet f -wave pairings. However, the authors assume that the Coulomb interaction is detrimental for superconductivity. In contrast, we find that the Coulomb interaction alone enables superconductivity, see also [25].

Here, we present a framework in which superconductivity in BBG emerges only from the long-range Coulomb interaction, arguably the simplest explanation. Due to screening by particle-hole pairs, this repulsive interaction between electrons becomes attractive and leads to pairing. We use a diagrammatic technique similar to the Kohn-Luttinger approach [28], which we have already applied to twisted bilayer and trilayer graphene [29, 30], as well as to RTG [15], thus allowing for a direct comparison of superconductivity in these systems and in BBG. We find superconductivity with critical temperature comparable to the experimental one [1], near the vHs. Including Ising SOC leads to significant increments in the critical temperature, as seen experimentally [4]. We observe that the order parameter (OP) changes sign within each valley. Adding a short-range Hubbard repulsion, we conclude that the OP also changes sign between valleys, showing that BBG is a spin-triplet superconductor. The rest of the paper is organized as follows: first we describe the continuum model and the Kohn-Luttinger-like framework for superconductivity. Then we present and discuss the results of the critical temperature, the superconducting OP and the positive effect of adding SOC.

The continuum model. Bernal bilayer graphene (BBG) refers to two stacked graphene layers so that atoms belonging to sublattice A of layer 1 lie over the atoms in sublattice B of layer 2. Similarly to monolayer graphene, BBG is a semi-metal in which the low energy bands touch at the Dirac points, but with parabolic instead of lin-

* alejandro.jimeno@imdea.org

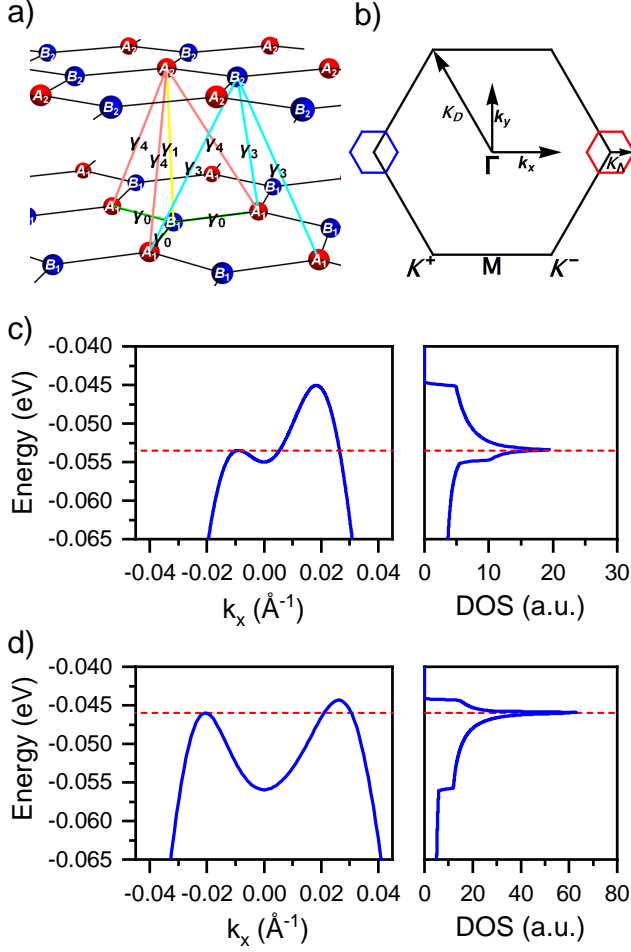


Figure 1. (a) Crystal lattice and hoppings of BBG. (b) Brillouin zone of BBG and RTG. We perform the calculation of superconductivity considering electron states in hexagonal grids around the Dirac points, with ultraviolet momentum cutoff $k_\Lambda = 0.025K_D$ for BBG (and $0.035K_D$ for RTG), with $K_D = 4\pi/3a$ the Dirac point modulus, which contain the Fermi surface and where the continuum model is a good approximation. Red and blue hexagons are plotted with $k_\Lambda = 0.2K_D$ for clarity. (c, d) Continuum model valence band and DOS of BBG and RTG with electric-field-induced gaps of 98 and 74 meV, respectively [31]. Dashed red lines mark the energies of the vHs.

ear dispersion [32, 33]. This band touching makes the charge susceptibility and other susceptibilities diverge [34], which leads to symmetry-broken phases [35–43], as seen in experiments [44–50]. A perpendicular electric field opens a gap and the bands acquire a ‘Mexican hat’ profile [51, 52], as shown in Fig. 1(c,d), making the density of states diverge logarithmically near the band edges, causing vHs and setting the stage for new correlated phenomena [1–4, 53–56].

In the continuum approximation the hamiltonian of BBG can be expressed in the basis $\{\Psi_{A_1}, \Psi_{B_1}, \Psi_{A_2}, \Psi_{B_2}\}$

as [52],

$$\mathcal{H}_\xi = \begin{pmatrix} V/2 & v_0\pi^\dagger & -v_4\pi^\dagger & v_3\pi \\ v_0\pi & V/2 + \Delta' & \gamma_1 & -v_4\pi^\dagger \\ -v_4\pi & \gamma_1 & -V/2 + \Delta' & v_0\pi^\dagger \\ v_3\pi^\dagger & -v_4\pi & v_0\pi & -V/2 \end{pmatrix}, \quad (1)$$

where $\pi = \xi p_x + ip_y$, $\xi = \pm 1$ is the valley index and $\mathbf{p} = \mathbf{k} - \mathbf{K}^\xi$ is the momentum with respect to the \mathbf{K}^ξ Dirac point, $v_i = \frac{\sqrt{3}a\gamma_i}{2\hbar}$ are effective velocities, a is the lattice constant and γ_i the different hoppings in the system, shown in Fig. 1(a). V corresponds to an applied electric field and Δ' is the energy difference between dimer (A_1, B_2) and non-dimer (A_2, B_1) sites. In Ref. [57] we list the values [52, 58], and describe the hamiltonian of RTG.

Kohn-Luttinger-like superconductivity. We propose that electronic interactions alone are enough to induce superconductivity in BBG and RTG and that the pairing glue is the screened long-range Coulomb potential V_{scr} . We employ a similar approach to the Kohn-Luttinger theory [28], following an analogous method as in [15]. We use the Random Phase Approximation to take into account the screened direct interaction to infinite order, while neglecting the contribution from the exchange interaction. The multiplicity of the direct diagrams equals the number of flavours, $N_f = 4$, so the approximation can be considered an expansion in powers of $1/N_f$. Under these assumptions the screened interaction is given by,

$$V_{scr}(\mathbf{q}) = \frac{V_C(\mathbf{q})}{1 - \Pi(\mathbf{q})V_C(\mathbf{q})}, \quad (2)$$

where $V_C(\mathbf{q}) = \frac{2\pi e^2}{\epsilon|\mathbf{q}|} \tanh(d|\mathbf{q}|)$ is the bare Coulomb potential, with e the electron charge, $\epsilon = 4$ the dielectric constant associated hBN encapsulation and $d = 40$ nm the distance to the metallic gate. $\Pi(\mathbf{q})$ corresponds to the zero-frequency limit of the charge susceptibility,

$$\Pi(\mathbf{q}) = \frac{N_f}{\Omega} \sum_{\mathbf{k}, m, n} \frac{f(\epsilon_{n,\mathbf{k}}) - f(\epsilon_{m,\mathbf{k}+\mathbf{q}})}{\epsilon_{n,\mathbf{k}} - \epsilon_{m,\mathbf{k}+\mathbf{q}}} |\langle \Psi_{m,\mathbf{k}+\mathbf{q}} | \Psi_{n,\mathbf{k}} \rangle|^2, \quad (3)$$

where m, n are band indexes, f is the Fermi-Dirac distribution and $\epsilon = E - \mu$ with μ being the Fermi energy, E are the eigenvalues, Ψ the eigenvectors of (1) and Ω is the area of the system. Once we perform this calculation within each valley, we include a short-range, repulsive Hubbard $U = 3$ eV [59, 60], which allows electrons to exchange valley and fixes the sign of the order parameter in each valley. We define the dimensionless anomalous expectation values in both valleys $\tilde{\Delta}^{+,i,j}(\mathbf{k}) = \langle c_{\mathbf{k},i,\mathbf{K}^+,\uparrow}^\dagger c_{-\mathbf{k},j,\mathbf{K}^-,\downarrow}^\dagger \rangle$ and $\tilde{\Delta}^{-,i,j}(\mathbf{k}) = \langle c_{\mathbf{k},i,\mathbf{K}^-,\uparrow}^\dagger c_{-\mathbf{k},j,\mathbf{K}^+,\downarrow}^\dagger \rangle$. Therefore the gap equation is

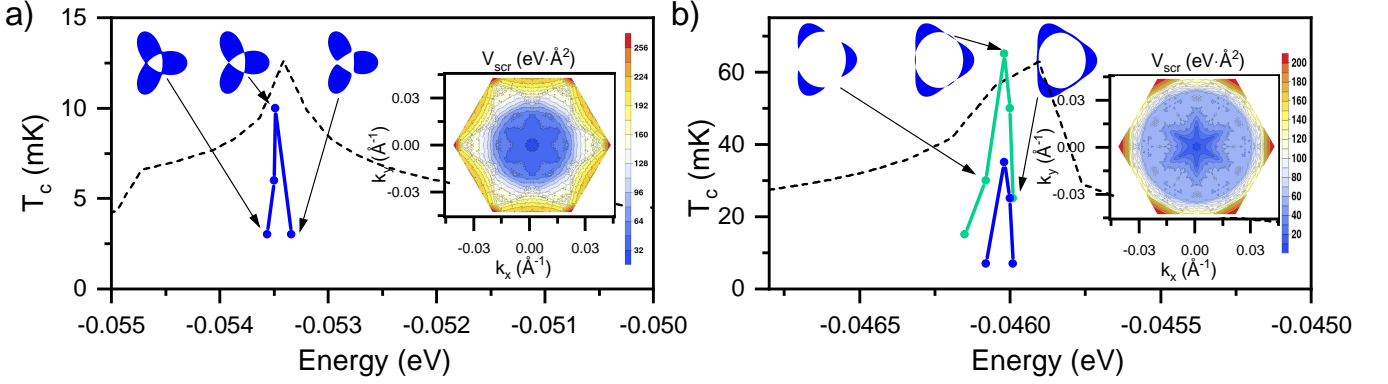


Figure 2. Superconducting critical temperature due to only the screened long-range Coulomb interaction (blue), and including also the short-range interaction (green), and DOS (a.u., dashed black) versus Fermi energy in (a) BBG with hole doping, near the vHs ($n_e \approx -0.87 \cdot 10^{12} \text{ cm}^{-2}$), we observe a $T_c \approx 10 \text{ mK}$, and (b) RTG with hole doping, near the vHs ($n_e \approx -0.6 \cdot 10^{12} \text{ cm}^{-2}$), $T_c \approx 33 \text{ mK}$ and it raises to $T_c \approx 65 \text{ mK}$ after including the short-range interaction. The top insets show the shape of the Fermi surfaces, which experience a change in topology at the vHs due to Lifshitz transitions. Right insets: screened Coulomb potential to k_Λ at the energy for which T_c is maximum.

given by,

$$\begin{aligned} \tilde{\Delta}^{+,i,j}(\mathbf{k}) = & -\frac{K_B T}{\Omega} \sum_{\mathbf{q}, \omega} \sum_{i', j'} \\ & V_{scr}(\mathbf{k} - \mathbf{q}) G_{\mathbf{K}^+}^{i, i'}(\mathbf{q}, i\omega) G_{\mathbf{K}^-}^{j, j'}(-\mathbf{q}, -i\omega) \tilde{\Delta}^{+,i', j'}(\mathbf{q}) \\ & + U G_{\mathbf{K}^-}^{i, i'}(\mathbf{q}, i\omega) G_{\mathbf{K}^+}^{j, j'}(-\mathbf{q}, -i\omega) \tilde{\Delta}^{-,j', i'}(-\mathbf{q}), \end{aligned} \quad (4)$$

where indexes i, j denote layer and sublattice degrees of freedom, ω is the Matsubara frequency and $G_{\mathbf{K}^\xi}^{i, j}(\mathbf{q}, i\omega)$ are electronic Green's functions. Eq. (4) can be understood in terms of the convolution of the gap with a kernel,

$$\tilde{\Delta}(\mathbf{k}) = \begin{pmatrix} \tilde{\Delta}^+(\mathbf{k}) \\ \tilde{\Delta}^-(\mathbf{k}) \end{pmatrix} = \sum_{\mathbf{k}'} \begin{pmatrix} \Gamma^+(\mathbf{k}, \mathbf{k}') & \tilde{U}(\mathbf{k}, \mathbf{k}') \\ \tilde{U}^\dagger(\mathbf{k}, \mathbf{k}') & \Gamma^-(\mathbf{k}, \mathbf{k}') \end{pmatrix} \tilde{\Delta}(\mathbf{k}'), \quad (5)$$

so that the solution of this gap equation is achieved when the maximum eigenvalue of the hermitian kernel reaches a value of 1, indicating the T_c at which the scattering amplitude for pairs of carriers of opposite momenta and energy within the Fermi surface has a pole. The corresponding eigenvector is the superconducting order parameter. The long-range Coulomb kernel is,

$$\Gamma_{m,n}^\xi(\mathbf{k}, \mathbf{k}') = -\frac{V_{scr}(\mathbf{k} - \mathbf{k}')}{\Omega} S_{m,n}^{\xi, \xi}(\mathbf{k}, \mathbf{k}') R_{m,m}^{\xi, \xi}(\mathbf{k}, \mathbf{k}') R_{n,n}^{\xi, \xi}(\mathbf{k}', \mathbf{k}'), \quad (6)$$

while the short-range kernel is,

$$\tilde{U}_{m,n}(\mathbf{k}, \mathbf{k}') = -\frac{U}{\Omega} S_{m,n}^{+, -}(\mathbf{k}, \mathbf{k}') R_{m,m}^{+, -}(\mathbf{k}, \mathbf{k}') R_{n,n}^{-, +}(\mathbf{k}', \mathbf{k}'), \quad (7)$$

with

$$R_{m,n}^{\xi, \xi'}(\mathbf{k}, \mathbf{k}') = \sqrt{\left(f(-\epsilon_{m,\mathbf{k}}^\xi) - f(\epsilon_{n,\mathbf{k}'}^{\xi'}) \right) / \left(\epsilon_{m,\mathbf{k}}^\xi + \epsilon_{n,\mathbf{k}'}^{\xi'} \right)}$$

and $S_{m,n}^{\xi, \xi'}(\mathbf{k}, \mathbf{k}') = \left| \left\langle \Psi_{m,\mathbf{k}}^\xi \left| \Psi_{n,\mathbf{k}'}^{\xi'} \right. \right\rangle \right|^2$. Once Eq. (5) is solved, gaps with dimensions of energy can be obtained as, $\Delta^+(\mathbf{k}) = V_{scr}(\mathbf{k}) \tilde{\Delta}^+(\mathbf{k}) + U \tilde{\Delta}^-(\mathbf{k})$ and $\Delta^-(\mathbf{k}) = V_{scr}(\mathbf{k}) \tilde{\Delta}^-(\mathbf{k}) + U \tilde{\Delta}^+(\mathbf{k})$.

Results. In Figure 2 we present the superconducting critical temperature of hole-doped BBG and RTG as a function of Fermi energy. We obtain a T_c of 10 mK for BBG and 65 mK for RTG, which match well with those observed experimentally [1, 9]. In both materials superconductivity survives only in narrow energy intervals around the vHs. It is worth noting that in RTG, including the short-range interaction doubles T_c , but it does not increase T_c in BBG. To obtain T_c , we use a \mathbf{k} -point density of up to $\mathcal{O}(10^7) \text{ \AA}^2$ for BBG and $\mathcal{O}(10^6) \text{ \AA}^2$ for RTG. Since states close to the Fermi surface give the principal contribution to Eq. (5), we cut off phase space by considering only states with $|\epsilon_{n,\mathbf{k}}| \leq 30 \text{ meV}$. These continuum model results are in good agreement with our previous tight-binding calculation for RTG [15]. The insets in Fig. 2 show the screened potential in momentum space, which is always repulsive, i.e. positive, and its value increases with increasing momentum. This dependence favors non s -wave superconductivity [61].

Moreover, inspired by the authors of Ref. [4], we study the effect of stacking a TMD on top of BBG. We assume that the main effect is an induced Ising spin-orbit coupling (SOC) in BBG, which breaks the equivalence between Cooper pairs $|\mathbf{K}^+, \uparrow; \mathbf{K}^-, \downarrow\rangle$ and $|\mathbf{K}^+, \downarrow; \mathbf{K}^-, \uparrow\rangle$, so the order parameter cannot be defined as a spin singlet or a spin triplet. The Ising hamiltonian which we add to (1) is just $\mathcal{H}_{I,\xi,s} = s \xi \lambda_I \mathbb{I}$, where s is the spin index. This interaction does not reshape the band structure, it just promotes one type of Cooper pair, by lowering the energy of two spin-valley flavours and raising that of the other two, splitting the original vHs into two. As shown in Figure 3, Ising SOC has a very positive effect on su-

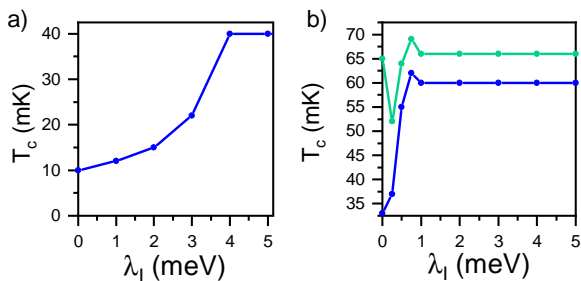


Figure 3. Ising spin-orbit coupling enhancement of critical temperature in hole-doped (a) BBG, for which T_c augments by a factor of 4 and saturates at $\lambda_I = 4$ meV. (b) RTG, for which T_c due to long-range interactions (blue) augments by a factor of 2 and saturates at $\lambda_I = 1$ meV. In contrast, Ising SOC is detrimental to short-range interactions, so T_c does not increase much when they are included (green).

perconductivity in both materials: it increases T_c by a factor of 4 in BBG, to 40 mK, congruent with the experiment, in which a factor of 10 increment was seen [4] and in RTG it brings forth a comparable increment of T_c due to long-range interactions only. The two vHs lead to two superconducting domes as a function of Fermi energy, as observed in Ref. [4], see [57]. It is worth noting that the spin-orbit enhancements of T_c saturate once the SOC fully polarizes the non-superconducting state into a half-metal [57].

Our model also yields the superconducting order parameters (OPs), shown in Figure 4. The OPs have structure within each valley: in BBG they display hotspots along the edges of the Fermi surface and sign changes along the edges of the Fermi surface. The sign is opposite for the inner and outer Fermi edges. In RTG, the maximum eigenvalue of the kernel is degenerate, leading to C_3 -symmetry breaking. Such degeneracy is not typical of conventional superconductors and hints at an exotic type of superconductivity. We observe that the OPs in both materials change sign between valleys, forming valley-singlets. Since the overall electron wavefunction must be antisymmetric, this implies that the pairs are spin-triplets. The order parameter that we find in the presence of spin-orbit coupling is similar to the spin-valley locking model in [62]. Our results are consistent with the phenomenological model discussed in [63].

Discussion. BBG and RTG are 2D superconductors with great structural stability and low disorder. These are decisive advantages to understand the physics at play, as they enable very reproducible experiments. There is also compelling evidence that both support spin-triplet superconducting phases and hence the pairing is most likely unconventional and mediated by electrons. Here, we show that a Kohn-Luttinger-like mechanism for superconductivity suffices to give rise to superconductivity in BBG and RTG, with critical temperatures in good agreement with experiments on both materials [1, 4, 9]. The screened long-range Coulomb interaction is the sole responsible for pairing. At fillings near the vHs, electron interactions

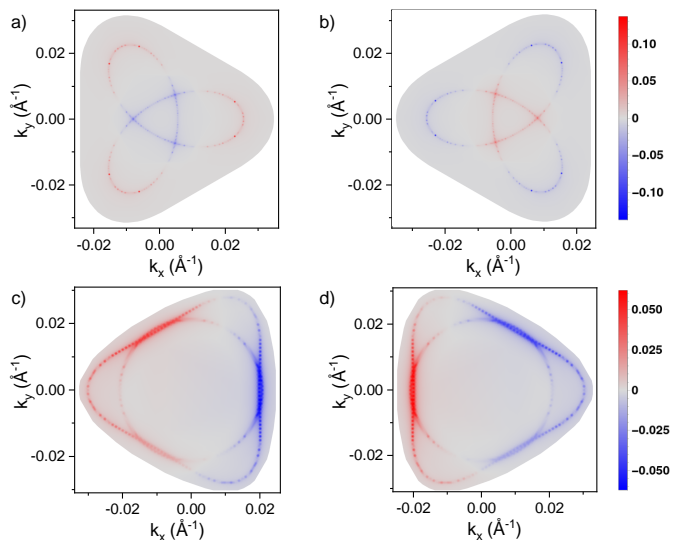


Figure 4. (a) Superconducting order parameter (OP) of BBG in valley K^+ , (b) in valley K^- , with hole doping and $T_c \approx 10$ mK. Within a single valley, the OP has hotspots along the edges of the Fermi surface and changes sign between the inner and outer edges. (c) OP of RTG in valley K^+ , (d) in valley K^- , with hole doping and $T_c \approx 65$ mK, showing intensity stripes along the edges of the Fermi surface. In both materials, the OP changes sign between valleys, which means that BBG and RTG are valley-singlet, spin-triplet superconductors.

strongly screen the Coulomb potential, which glues pairs of carriers, one in each valley, and causes superconductivity. Of course, other excitations may dress the Coulomb interaction and contribute to superconductivity in BBG [24–26] and RTG [10–14, 16–20].

Furthermore, our results support the proposal in Ref. [4] that Ising SOC is what causes the enhancement of T_c in BBG when the TMD WSe_2 is stacked on top of it. Based on the results presented here, we predict that the same idea will boost superconductivity in RTG by a comparable amount as in BBG. Since the four times increment we obtain in BBG underestimates the ten times increment observed in the experiment, it is likely that our result for RTG similarly underestimates the SOC enhancement that superconductivity will experience in this material. Hence, we conjecture that RTG with WSe_2 stacked on top will reach $T_c \sim 1$ K, putting it on par with magic-angle twisted bilayer graphene and the other twisted stacks [64–70].

The OPs reveal two key aspects of superconductivity. First, the OPs show sign changes within each valley, which are characteristic of weak coupling superconductivity, in which electrons interact and form pairs with high angular momentum, such as those with p -wave or f -wave symmetry. Another consequence of this intravalley structure is that long-range disorder will suppress superconductivity in these materials, unlike in twisted stacks. Second, the sign of the OPs changes between valleys, hence the pairs are spin-triplets.

In BBG and RTG, the screened long-range Coulomb interaction suffices to reach critical temperatures that agree with experiments, while in twisted stacks it is necessary to include Umklapp processes involving large momentum transfers and dressing by phonons, pointing to a rich interplay between interactions and wavefunction complexity [29, 30]. Also, the rigidity of the bands of BBG and RTG leads to narrow superconducting sleeves, because the phase vanishes when the Fermi energy passes the vHs. In contrast, in twisted stacks the bands reshape with filling and there is a pinning of the Fermi energy to the vHs [71], allowing for wide superconducting domes.

In conclusion, we find that superconductivity emerges in BBG and RTG from the screened long-range Coulomb interaction alone. This proposal, based on Kohn-Luttinger theory, yields results consistent with three major experimental advances [1, 4, 9]. We observe critical

temperatures that agree with experiments. The inclusion of Ising SOC results in prominent increments in critical temperature for both materials, in harmony with the experimental observation in BBG. In the absence of Ising SOC the OPs show that both materials are valley-singlet, spin-triplet superconductors, while this classification cannot be applied when SOC is present since it locks the spin and valley degrees of freedom.

Acknowledgments. We are thankful to A. V. Chubukov for illuminating discussions. We acknowledge support from the Severo Ochoa programme for centres of excellence in R&D (Grant No. SEV-2016-0686, Ministerio de Ciencia e Innovación, Spain); from the European Commission, within the Graphene Flagship, Core 3, grant number 881603 and from grants NMAT2D (Comunidad de Madrid, Spain) and SprQuMat (Ministerio de Ciencia e Innovación, Spain).

-
- [1] H. Zhou, L. Holleis, Y. Saito, L. Cohen, W. Huynh, C. L. Patterson, F. Yang, T. Taniguchi, K. Watanabe, and A. F. Young, Isospin magnetism and spin-polarized superconductivity in bernal bilayer graphene, *Science* **375**, 774 (2022).
- [2] S. C. de la Barrera, S. Aronson, Z. Zheng, K. Watanabe, T. Taniguchi, Q. Ma, P. Jarillo-Herrero, and R. Ashoori, Cascade of isospin phase transitions in bernal-stacked bilayer graphene at zero magnetic field, *Nature Physics* **18**, 771 (2022).
- [3] A. M. Seiler, F. R. Geisenhof, F. Winterer, K. Watanabe, T. Taniguchi, T. Xu, F. Zhang, and R. T. Weitz, Quantum cascade of correlated phases in trigonally warped bilayer graphene, *Nature* **608**, 298 (2022).
- [4] Y. Zhang, R. Polski, A. Thomson, É. Lantagne-Hurtubise, C. Lewandowski, H. Zhou, K. Watanabe, T. Taniguchi, J. Ali, and S. Nadj-Perge, Spin-orbit enhanced superconductivity in bernal bilayer graphene, arXiv preprint [arXiv:2205.05087](https://arxiv.org/abs/2205.05087) 10.48550/arXiv.2205.05087 (2022).
- [5] C. N. Lau, M. W. Bockrath, K. F. Mak, and F. Zhang, Reproducibility in the fabrication and physics of moiré materials, *Nature* **602**, 41 (2022).
- [6] A. Uri, S. Grover, Y. Cao, J. A. Crosse, K. Bagani, D. Rodan-Legrain, Y. Myasoedov, K. Watanabe, T. Taniguchi, P. Moon, M. Koshino, P. Jarillo-Herrero, and E. Zeldov, Mapping the twist-angle disorder and Landau levels in magic-angle graphene, *Nature* **581**, 47 (2020).
- [7] A. Schäpers, J. Sonntag, L. Valerius, B. Pestka, J. Strassdas, K. Watanabe, T. Taniguchi, L. Wirtz, M. Morgenstern, B. Beschoten, R. J. Dolleman, and C. Stampfer, Raman imaging of twist angle variations in twisted bilayer graphene at intermediate angles, *2D Materials* **9**, 045009 (2022).
- [8] N. P. Kazmierczak, M. V. Winkle, C. Ophus, K. C. Bustillo, S. Carr, H. G. Brown, J. Ciston, T. Taniguchi, K. Watanabe, and D. K. Bediako, Strain fields in twisted bilayer graphene, *Nature Materials* **20**, 956 (2021).
- [9] H. Zhou, T. Xie, T. Taniguchi, K. Watanabe, and A. F. Young, Superconductivity in rhombohedral trilayer graphene, *Nature* **598**, 434 (2021).
- [10] Y.-Z. Chou, F. Wu, J. D. Sau, and S. D. Sarma, Acoustic-phonon-mediated superconductivity in rhombohedral trilayer graphene, *Physical Review Letters* **127**, 10.1103/physrevlett.127.187001 (2021).
- [11] H. Dai, J. Hou, X. Zhang, Y. Liang, and T. Ma, Mott insulating state and d+id superconductivity in an abc graphene trilayer, *Physical Review B* **104**, 10.1103/physrevb.104.035104 (2021).
- [12] Z. Dong and L. Levitov, Superconductivity in the vicinity of an isospin-polarized state in a cubic Dirac band, arXiv preprint [arXiv:2109.01133](https://arxiv.org/abs/2109.01133) 10.48550/arxiv.2109.01133 (2021).
- [13] A. Ghazaryan, T. Holder, M. Serbyn, and E. Berg, Unconventional superconductivity in systems with annular Fermi surfaces: Application to rhombohedral trilayer graphene, *Physical Review Letters* **127**, 10.1103/physrevlett.127.247001 (2021).
- [14] S. Chatterjee, T. Wang, E. Berg, and M. P. Zaletel, Intervalley coherent order and isospin fluctuation mediated superconductivity in rhombohedral trilayer graphene, *Nature Communications* **13**, 10.1038/s41467-022-33561-w (2022).
- [15] T. Cea, P. A. Pantaleón, V. T. Phong, and F. Guinea, Superconductivity from repulsive interactions in rhombohedral trilayer graphene: A Kohn-Luttinger-like mechanism, *Physical Review B* **105**, 10.1103/physrevb.105.075432 (2022).
- [16] Y.-Z. You and A. Vishwanath, Kohn-Luttinger superconductivity and intervalley coherence in rhombohedral trilayer graphene, *Physical Review B* **105**, 10.1103/physrevb.105.134524 (2022).
- [17] A. L. Szabó and B. Roy, Metals, fractional metals, and superconductivity in rhombohedral trilayer graphene, *Physical Review B* **105**, 10.1103/physrevb.105.1081407 (2022).
- [18] W. Qin, C. Huang, T. Wolf, N. Wei, I. Blinov, and A. H. MacDonald, Functional renormalization group study of superconductivity in rhombohedral trilayer graphene, arXiv preprint [arXiv:2203.09083](https://arxiv.org/abs/2203.09083) 10.48550/arxiv.2203.09083 (2022).

- [19] H. Dai, R. Ma, X. Zhang, and T. Ma, Quantum monte carlo study of superconductivity in rhombohedral trilayer graphene under an electric field, arXiv preprint [arXiv:2204.06222](https://arxiv.org/abs/2204.06222) [10.48550/arxiv.2204.06222](https://doi.org/10.48550/arxiv.2204.06222) (2022).
- [20] D.-C. Lu, T. Wang, S. Chatterjee, and Y.-Z. You, Correlated metals and unconventional superconductivity in rhombohedral trilayer graphene: A renormalization group analysis, *Physical Review B* **106**, [10.1103/physrevb.106.155115](https://doi.org/10.1103/physrevb.106.155115) (2022).
- [21] U. Zondiner, A. Rozen, D. Rodan-Legrain, Y. Cao, R. Queiroz, T. Taniguchi, K. Watanabe, Y. Oreg, F. von Oppen, A. Stern, E. Berg, P. Jarillo-Herrero, and S. Ilani, Cascade of phase transitions and dirac revivals in magic-angle graphene, *Nature* **582**, 203 (2020).
- [22] D. Wong, K. P. Nuckolls, M. Oh, B. Lian, Y. Xie, S. Jeon, K. Watanabe, T. Taniguchi, B. A. Bernevig, and A. Yazdani, Cascade of electronic transitions in magic-angle twisted bilayer graphene, *Nature* **582**, 198 (2020).
- [23] H. Zhou, T. Xie, A. Ghazaryan, T. Holder, J. R. Ehrets, E. M. Spanton, T. Taniguchi, K. Watanabe, E. Berg, M. Serbyn, and A. F. Young, Half- and quarter-metals in rhombohedral trilayer graphene, *Nature* **598**, 429 (2021).
- [24] A. L. Szabó and B. Roy, Competing orders and cascade of degeneracy lifting in doped bernal bilayer graphene, *Phys. Rev. B* **105**, L201107 (2022).
- [25] Z. Dong, A. V. Chubukov, and L. Levitov, Spin-triplet superconductivity at the onset of isospin order in biased bilayer graphene, arXiv preprint [arXiv:2205.13353](https://arxiv.org/abs/2205.13353) [10.48550/arxiv.2205.13353](https://doi.org/10.48550/arxiv.2205.13353) (2022).
- [26] Y.-Z. Chou, F. Wu, J. D. Sau, and S. D. Sarma, Acoustic-phonon-mediated superconductivity in bernal bilayer graphene, *Physical Review B* **105**, [10.1103/physrevb.105.1100503](https://doi.org/10.1103/physrevb.105.1100503) (2022).
- [27] Y.-Z. Chou, F. Wu, and S. D. Sarma, Enhanced superconductivity through virtual tunneling in bernal bilayer graphene coupled to wse 2 , *Physical Review B* **106**, [10.1103/physrevb.106.1180502](https://doi.org/10.1103/physrevb.106.1180502) (2022).
- [28] W. Kohn and J. M. Luttinger, New mechanism for superconductivity, *Physical Review Letters* **15**, 524 (1965).
- [29] T. Cea and F. Guinea, Coulomb interaction, phonons, and superconductivity in twisted bilayer graphene, *Proceedings of the National Academy of Sciences* **118**, [10.1073/pnas.2107874118](https://doi.org/10.1073/pnas.2107874118) (2021).
- [30] V. T. Phong, P. A. Pantaleón, T. Cea, and F. Guinea, Band structure and superconductivity in twisted trilayer graphene, *Physical Review B* **104**, [10.1103/physrevb.104.1121116](https://doi.org/10.1103/physrevb.104.1121116) (2021).
- [31] To open these gaps one need to include electric fields of around $V = 110$ meV and $V = 42.5$ meV, respectively. It is worth noting that there is considerable uncertainty in the relation between the applied fields and the gaps, see Refs. [51, 72].
- [32] E. McCann and V. I. Fal'ko, Landau-level degeneracy and quantum hall effect in a graphite bilayer, *Physical Review Letters* **96**, [10.1103/physrevlett.96.086805](https://doi.org/10.1103/physrevlett.96.086805) (2006).
- [33] K. S. Novoselov, E. McCann, S. V. Morozov, V. I. Fal'ko, M. I. Katsnelson, U. Zeitler, D. Jiang, F. Schedin, and A. K. Geim, Unconventional quantum hall effect and berry's phase of 2π in bilayer graphene, *Nature Physics* **2**, 177 (2006).
- [34] J. Nilsson, A. H. C. Neto, N. M. R. Peres, and F. Guinea, Electron-electron interactions and the phase diagram of a graphene bilayer, *Physical Review B* **73**, [10.1103/physrevb.73.214418](https://doi.org/10.1103/physrevb.73.214418) (2006).
- [35] F. Zhang, J. Jung, G. A. Fiete, Q. Niu, and A. H. MacDonald, Spontaneous quantum hall states in chirally stacked few-layer graphene systems, *Phys. Rev. Lett.* **106**, 156801 (2011).
- [36] H. Min, G. Borghi, M. Polini, and A. H. MacDonald, Pseudospin magnetism in graphene, *Physical Review B* **77**, [10.1103/physrevb.77.041407](https://doi.org/10.1103/physrevb.77.041407) (2008).
- [37] O. Vafek, Interacting fermions on the honeycomb bilayer: From weak to strong coupling, *Physical Review B* **82**, [10.1103/physrevb.82.205106](https://doi.org/10.1103/physrevb.82.205106) (2010).
- [38] O. Vafek and K. Yang, Many-body instability of coulomb interacting bilayer graphene: Renormalization group approach, *Physical Review B* **81**, [10.1103/physrevb.81.041401](https://doi.org/10.1103/physrevb.81.041401) (2010).
- [39] R. Nandkishore and L. Levitov, Dynamical screening and excitonic instability in bilayer graphene, *Physical Review Letters* **104**, [10.1103/physrevlett.104.156803](https://doi.org/10.1103/physrevlett.104.156803) (2010).
- [40] Y. Lemonik, I. Aleiner, and V. I. Fal'ko, Competing nematic, antiferromagnetic, and spin-flux orders in the ground state of bilayer graphene, *Physical Review B* **85**, [10.1103/physrevb.85.245451](https://doi.org/10.1103/physrevb.85.245451) (2012).
- [41] F. Zhang and A. H. MacDonald, Distinguishing spontaneous quantum hall states in bilayer graphene, *Physical Review Letters* **108**, [10.1103/physrevlett.108.186804](https://doi.org/10.1103/physrevlett.108.186804) (2012).
- [42] V. Cvetkovic, R. E. Throckmorton, and O. Vafek, Electronic multicriticality in bilayer graphene, *Physical Review B* **86**, [10.1103/physrevb.86.075467](https://doi.org/10.1103/physrevb.86.075467) (2012).
- [43] J. Martin, B. E. Feldman, R. T. Weitz, M. T. Allen, and A. Yacoby, Local compressibility measurements of correlated states in suspended bilayer graphene, *Physical Review Letters* **105**, [10.1103/physrevlett.105.256806](https://doi.org/10.1103/physrevlett.105.256806) (2010).
- [44] R. T. Weitz, M. T. Allen, B. E. Feldman, J. Martin, and A. Yacoby, Broken-symmetry states in doubly gated suspended bilayer graphene, *Science* **330**, 812 (2010).
- [45] A. S. Mayorov, D. C. Elias, M. Mucha-Kruczynski, R. V. Gorbachev, T. Tudorovskiy, A. Zhukov, S. V. Morozov, M. I. Katsnelson, A. K. Geim, and K. S. N. and, Interaction-driven spectrum reconstruction in bilayer graphene, *Science* **333**, 860 (2011).
- [46] J. Velasco, L. Jing, W. Bao, Y. Lee, P. Kratz, V. Aji, M. Bockrath, C. N. Lau, C. Varma, R. Stillwell, D. Smirnov, F. Zhang, J. Jung, and A. H. MacDonald, Transport spectroscopy of symmetry-broken insulating states in bilayer graphene, *Nature Nanotechnology* **7**, 156 (2012).
- [47] F. Freitag, J. Trbovic, M. Weiss, and C. Schönenberger, Spontaneously gapped ground state in suspended bilayer graphene, *Physical Review Letters* **108**, [10.1103/physrevlett.108.076602](https://doi.org/10.1103/physrevlett.108.076602) (2012).
- [48] L. Ju, Z. Shi, N. Nair, Y. Lv, C. Jin, J. Velasco, C. Ojeda-Aristizabal, H. A. Bechtel, M. C. Martin, A. Zettl, J. Analytis, and F. Wang, Topological valley transport at bilayer graphene domain walls, *Nature* **520**, 650 (2015).
- [49] J. I. A. Li, C. Tan, S. Chen, Y. Zeng, T. Taniguchi, K. Watanabe, J. Hone, and C. R. Dean, Even-denominator fractional quantum hall states in bilayer graphene, *Science* **358**, 648 (2017).
- [50] A. A. Zibrov, C. Kometter, H. Zhou, E. M. Spanton, T. Taniguchi, K. Watanabe, M. P. Zaletel, and A. F. Young, Tunable interacting composite fermion phases in a half-filled bilayer-graphene landau level, *Nature* **549**, 360 (2017).

- [51] Y. Zhang, T.-T. Tang, C. Girit, Z. Hao, M. C. Martin, A. Zettl, M. F. Crommie, Y. R. Shen, and F. Wang, Direct observation of a widely tunable bandgap in bilayer graphene, *Nature* **459**, 820 (2009).
- [52] E. McCann and M. Koshino, The electronic properties of bilayer graphene, *Reports on Progress in Physics* **76**, 056503 (2013).
- [53] P. Maher, L. Wang, Y. Gao, C. Forsythe, T. Taniguchi, K. Watanabe, D. Abanin, Z. Papić, P. Cadden-Zimansky, J. Hone, P. Kim, and C. R. Dean, Tunable fractional quantum hall phases in bilayer graphene, *Science* **345**, 61 (2014).
- [54] K. Lee, B. Fallahazad, J. Xue, D. C. Dillen, K. Kim, T. Taniguchi, K. Watanabe, and E. Tutuc, Chemical potential and quantum hall ferromagnetism in bilayer graphene, *Science* **345**, 58 (2014).
- [55] A. Kou, B. E. Feldman, A. J. Levin, B. I. Halperin, K. Watanabe, T. Taniguchi, and A. Yacoby, Electron-hole asymmetric integer and fractional quantum hall effect in bilayer graphene, *Science* **345**, 55 (2014).
- [56] F. R. Geisenhof, F. Winterer, A. M. Seiler, J. Lenz, T. Xu, F. Zhang, and R. T. Weitz, Quantum anomalous hall octet driven by orbital magnetism in bilayer graphene, *Nature* **598**, 53 (2021).
- [57] See supplementary information, which includes Refs. [73, 74].
- [58] See Ref. [75] for a revised version of the parameters of BBG.
- [59] T. O. Wehling, E. Şaşıoğlu, C. Friedrich, A. I. Lichtenstein, M. I. Katsnelson, and S. Blügel, Strength of effective coulomb interactions in graphene and graphite, *Phys. Rev. Lett.* **106**, 236805 (2011).
- [60] M. Schüler, M. Rösner, T. O. Wehling, A. I. Lichtenstein, and M. I. Katsnelson, Optimal hubbard models for materials with nonlocal coulomb interactions: Graphene, silicene, and benzene, *Phys. Rev. Lett.* **111**, 036601 (2013).
- [61] S. Maiti and A. V. Chubukov, Superconductivity from repulsive interaction, in *AIP Conference Proceedings*, Vol. 1550 (2013) p. 3.
- [62] E. Lake, A. S. Patri, and T. Senthil, Pairing symmetry of twisted bilayer graphene: A phenomenological synthesis, *Phys. Rev. B* **106**, 104506 (2022).
- [63] J. B. Curtis, N. R. Poniatowski, Y. Xie, A. Yacoby, E. Demler, and P. Narang, Stabilizing fluctuating spin-triplet superconductivity in graphene via induced spin-orbit coupling, arXiv preprint [arXiv:2209.10560](https://arxiv.org/abs/2209.10560) (2022).
- [64] Y. Cao, V. Fatemi, S. Fang, K. Watanabe, T. Taniguchi, E. Kaxiras, and P. Jarillo-Herrero, Unconventional superconductivity in magic-angle graphene superlattices, *Nature* **556**, 43 (2018).
- [65] M. Yankowitz, S. Chen, H. Polshyn, Y. Zhang, K. Watanabe, T. Taniguchi, D. Graf, A. F. Young, and C. R. Dean, Tuning superconductivity in twisted bilayer graphene, *Science* **363**, 1059 (2019).
- [66] X. Lu, P. Stepanov, W. Yang, M. Xie, M. A. Aamir, I. Das, C. Urgell, K. Watanabe, T. Taniguchi, G. Zhang, A. Bachtold, A. H. MacDonald, and D. K. Efetov, Superconductors, orbital magnets and correlated states in magic-angle bilayer graphene, *Nature* **574**, 653 (2019).
- [67] J. M. Park, Y. Cao, K. Watanabe, T. Taniguchi, and P. Jarillo-Herrero, Tunable strongly coupled superconductivity in magic-angle twisted trilayer graphene, *Nature* **590**, 249 (2021).
- [68] Z. Hao, A. M. Zimmerman, P. Ledwith, E. Khalaf, D. H. Najafabadi, K. Watanabe, T. Taniguchi, A. Vishwanath, and P. Kim, Electric field-tunable superconductivity in alternating-twist magic-angle trilayer graphene, *Science* **371**, 1133 (2021).
- [69] Y. Zhang, R. Polski, C. Lewandowski, A. Thomson, Y. Peng, Y. Choi, H. Kim, K. Watanabe, T. Taniguchi, J. Alicea, F. von Oppen, G. Refael, and S. Nadj-Perge, Promotion of superconductivity in magic-angle graphene multilayers, *Science* **377**, 1538 (2022).
- [70] J. M. Park, Y. Cao, L.-Q. Xia, S. Sun, K. Watanabe, T. Taniguchi, and P. Jarillo-Herrero, Robust superconductivity in magic-angle multilayer graphene family, *Nature Materials* **21**, 877 (2022).
- [71] T. Cea, N. R. Walet, and F. Guinea, Electronic band structure and pinning of fermi energy to van hove singularities in twisted bilayer graphene: A self-consistent approach, *Phys. Rev. B* **100**, 205113 (2019).
- [72] C. H. Lui, Z. Li, K. F. Mak, E. Cappelluti, and T. F. Heinz, Observation of an electrically tunable band gap in trilayer graphene, *Nature Physics* **7**, 944 (2011).
- [73] F. Zhang, B. Sahu, H. Min, and A. H. MacDonald, Band structure of *abc*-stacked graphene trilayers, *Phys. Rev. B* **82**, 035409 (2010).
- [74] A. A. Zibrov, P. Rao, C. Kometter, E. M. Spanton, J. I. A. Li, C. R. Dean, T. Taniguchi, K. Watanabe, M. Serbyn, and A. F. Young, Emergent dirac gullies and gully-symmetry-breaking quantum hall states in *aba* trilayer graphene, *Phys. Rev. Lett.* **121**, 167601 (2018).
- [75] J. Jung and A. H. MacDonald, Accurate tight-binding models for the π bands of bilayer graphene, *Phys. Rev. B* **89**, 035405 (2014).

Supplementary information for ‘Superconductivity from electronic interactions and spin-orbit enhancement in bilayer and trilayer graphene’

I. THE CONTINUUM MODEL OF BBG AND RTG

Bernal bilayer graphene (BBG) refers to two vertically stacked graphene layers so that atoms belonging to the sublattice A of layer 1 lie over the atoms of the sublattice B of layer 2, while rhombohedral trilayer graphene (RTG) alludes to a stack of three layers in which the atoms of sublattice A of layer 3 are located over the atoms of sublattice B of layer 2 while the atoms of sublattice A of this layer lie over the atoms of sublattice B of layer 1.

Similar to monolayer graphene, BBG and RTG are semi-metals with band touching at the Dirac points in the low energy region, but with parabolic instead of linear dispersion [32, 33]. An external perpendicular electric field opens a gap in both systems and the low energy bands nearly flatten around the Dirac points while acquiring ‘Mexican hat’ profiles [52], as can be seen in Fig. 1(c,d) in the main text. The flattening of the low energy bands leads to logarithmic divergences in the densities of states which correspond to van Hove singularities (vHs).

In real space the BBG and RTG unit cell is defined by vectors $\mathbf{a}_1 = \frac{a}{2}(1, \sqrt{3})$ and $\mathbf{a}_2 = \frac{a}{2}(1, -\sqrt{3})$, where $a = 2.46\text{\AA}$ is the graphene lattice constant. The Brillouin zone (BZ) of both systems is defined by the reciprocal lattice vectors $\mathbf{b}_1 = \frac{2\pi}{a}(1, \frac{1}{\sqrt{3}})$ and $\mathbf{b}_2 = \frac{2\pi}{a}(1, -\frac{1}{\sqrt{3}})$. In the continuum approximation the hamiltonian of BBG can be expressed in the basis $\{\Psi_{A_1}, \Psi_{B_1}, \Psi_{A_2}, \Psi_{B_2}\}$ as follows from [52],

$$\mathcal{H}_{BBG} = \begin{pmatrix} V/2 & v_0\pi^\dagger & -v_4\pi^\dagger & v_3\pi \\ v_0\pi & V/2 + \Delta' & \gamma_1 & -v_4\pi^\dagger \\ -v_4\pi & \gamma_1 & -V/2 + \Delta' & v_0\pi^\dagger \\ v_3\pi^\dagger & -v_4\pi & v_0\pi & -V/2 \end{pmatrix}, \quad (\text{S1})$$

In the case of RTG, the hamiltonian in the basis $\{\Psi_{A_1}, \Psi_{B_1}, \Psi_{A_2}, \Psi_{B_2}, \Psi_{A_3}, \Psi_{B_3}\}$ takes the following form, see [73],

$$\mathcal{H}_{RTG} = \begin{pmatrix} V + \Delta_2 + \delta & v_0\pi^\dagger & v_4\pi^\dagger & v_3\pi & 0 & \gamma_2/2 \\ v_0\pi & V + \Delta_2 & \gamma_1 & v_4\pi^\dagger & 0 & 0 \\ v_4\pi & \gamma_1 & -2\Delta_2 & v_0\pi^\dagger & v_4\pi^\dagger & v_3\pi \\ v_3\pi^\dagger & v_4\pi & v_0\pi & -2\Delta_2 & \gamma_1 & v_4\pi^\dagger \\ 0 & 0 & v_4\pi & \gamma_1 & -V + \Delta_2 & v_0\pi^\dagger \\ \gamma_2/2 & 0 & v_3\pi^\dagger & v_4\pi & v_0\pi & -V + \Delta_2 + \delta \end{pmatrix}, \quad (\text{S2})$$

with $\gamma_0 = 3.1$, eV, $\gamma_1 = 0.38$ eV, $\gamma_2 = -0.015$ eV, $\gamma_3 = -0.29$ eV, $\gamma_4 = -0.141$ eV, $\delta = -0.015$ eV and $\Delta_2 = -0.0023$ eV, extracted from [23, 74]. In order to set an ultraviolet momentum cutoff k_Λ , we compare the low energy band

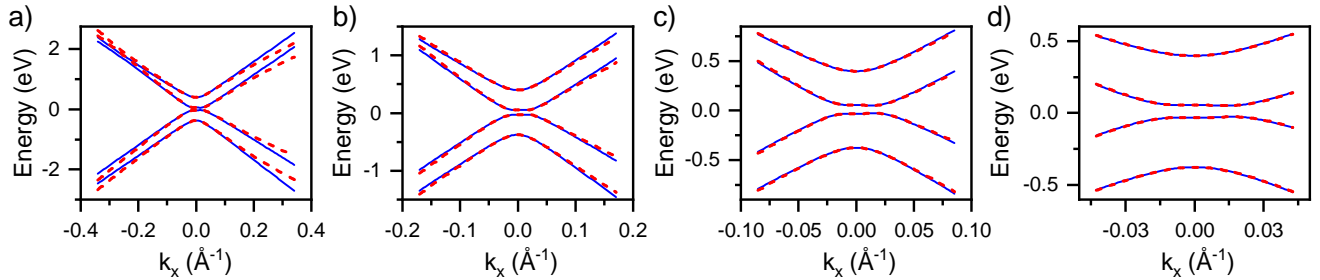


Figure S1. Comparison between tight-binding (dotted red) and continuum model (solid blue) low energy band structure of BBG near the Dirac point for (a) $k_\Lambda = 0.2$, (b) $k_\Lambda = 0.1$, (c) $k_\Lambda = 0.05$ and (d) $k_\Lambda = 0.025$, in units of δK_D .

structure of BBG within the tight-binding and continuum models, which can be seen in Fig. S1, Ref. [15] shows a similar comparison for RTG. We observe that for $k_\Lambda \leq 0.05K_D$, where $K_D = 4\pi/3a$ is the modulus of the Dirac point momentum, both models are in good agreement. The idea is to choose the lowest possible k_Λ , such that there is a high density of \mathbf{k} -points near the Fermi surface, and the energy resolution of the calculation allows for the determination of the critical temperature even if it is low. To find a convergent T_c , an energy resolution of $K_B T_c$ is required, where K_B is the Boltzmann constant. However, there is a lower bound on k_Λ . This is because superconductivity comes from kernel matrix elements that involve scatterings with momentum exchange $\mathbf{q} = \mathbf{k} - \mathbf{k}'$, in which \mathbf{k} and \mathbf{k}' are within

the Fermi surface. Therefore, it is necessary to set $k_\Lambda > \max|\mathbf{q}|$, in order to calculate the screened potential for all relevant momentum values. For the displacement fields studied in the main text, $k_\Lambda = 0.025K_D$ suffices for the bilayer, while the trilayer requires $k_\Lambda = 0.035K_D$. It is worth noting that the size of the Fermi surface near the vHs, and hence the adequate k_Λ , increase with displacement field.

II. REAL SPACE SCREENED COULOMB POTENTIAL

A cut along the x -direction of the screened Coulomb potential in real space is shown in Fig. S2. For this, we compute the Fourier transform of the potential via,

$$V(\mathbf{r}) = \Delta_{\mathbf{k}}^2 \sum_{\mathbf{k}} V_{scr}(\mathbf{k}) e^{-i\mathbf{k}\cdot\mathbf{r}}, \quad (\text{S3})$$

where $\Delta_{\mathbf{k}}$ is the spacing between adjacent points in \mathbf{k} -space. As can be seen in Fig. S2, the repulsive Coulomb potential

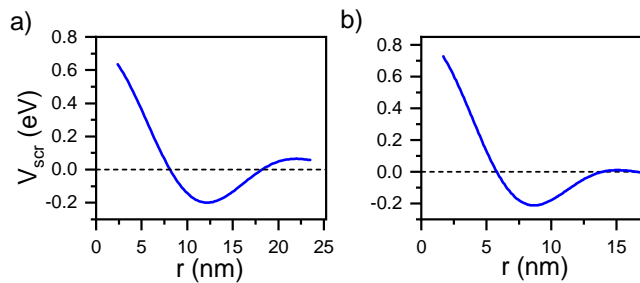


Figure S2. Real space cut along the x -direction of the screened Coulomb potential. (a) in BBG near the hole-doped vHs at $T = 10$ mK. (b) in RTG near the hole-doped vHs at $T = 65$ mK.

develops into an effective attractive potential once the screening is taken into consideration at a temperature around the T_c of BBG and RTG. Since the continuum model yields the correct electronic properties up to a cutoff in the reciprocal space defined by k_Λ , we think that the position of the minimum of the screened potential is overestimated as the short-range information cannot be well captured with this model, and the magnitude is also unreliable. However, it is good enough to qualitatively describe the appearance of an attractive potential region which promotes superconductivity.

III. ISING SPIN-ORBIT COUPLING

To account for the effects induced in the BBG by the proximity of WSe₂ and following the ideas introduced in [4], we include Ising spin-orbit coupling (SOC) to check if it can give rise to an enhancement of the critical temperature as measured experimentally. The Ising SOC results in an energy imbalance between Cooper pairs $|\mathbf{K}^+, \uparrow; \mathbf{K}^-, \downarrow\rangle$ and $|\mathbf{K}^+, \downarrow; \mathbf{K}^-, \uparrow\rangle$, making one of them to rise in energy by a quantity given by the SOC strength parameter, λ_I , while lowering the other by the same amount. Thus, the spin-valley-dependent hamiltonian for Ising SOC is given by,

$$\mathcal{H}_{I,\xi,s} = s\xi\lambda_I\mathbb{I}, \quad (\text{S4})$$

where \mathbb{I} is the identity matrix. As can be inferred from Eq. (S4) and seen in Figure S4, Ising SOC locks the spin and valley degrees of freedom in the OP, making inapplicable the classification as spin-singlet or spin-triplet.

In the presence of SOC, the original vHs at μ_0 , which is four-fold degenerate, splits into two vHs which are two-fold degenerate, separated by $2\lambda_I$. A practical consequence is that the susceptibility in Eq. 3 in the main text needs to be separated in two parts, each with a prefactor of $N_f = 2$, which are then summed to give the total susceptibility. Regarding the screening of the Coulomb potential, in reciprocal space, increasing the strength of Ising SOC narrows the region around the Dirac point where the minimum of the screened potential is concentrated, and makes it grow faster as a function of momentum. In real space this directly translates into a more attractive potential, see Fig. S3, which is consistent with the increment in critical temperature shown in Fig. 3 in the main text. The saturation of the critical temperature corresponds to the saturation of the minimum of the screened potential in real space, as reflected in Table I.

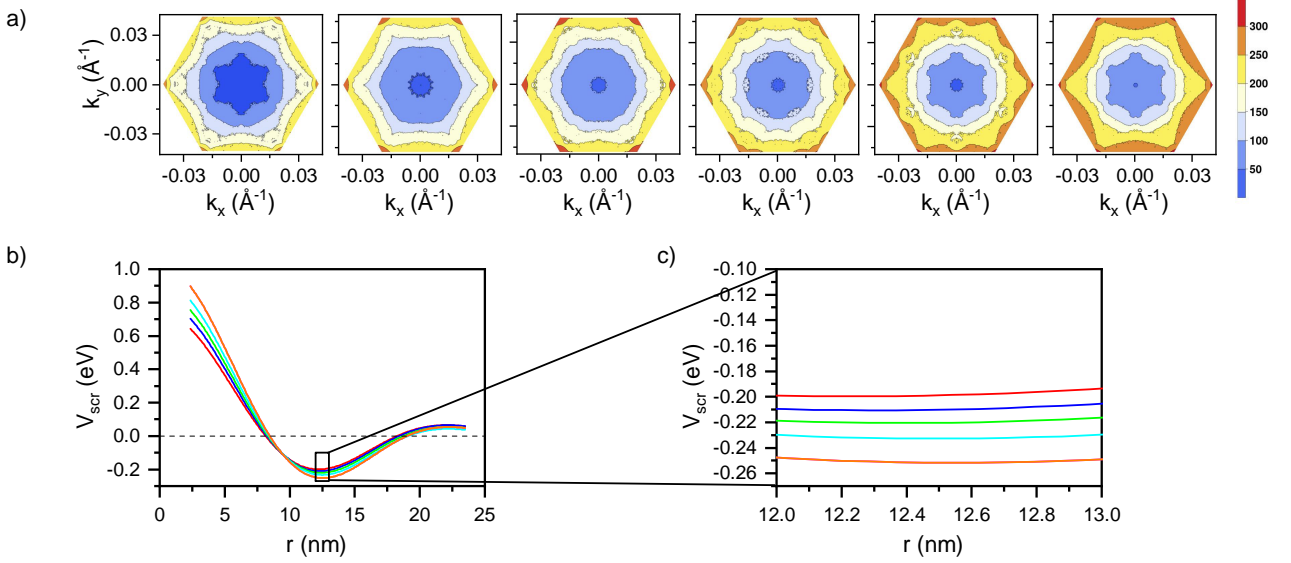


Figure S3. (a) Screened potential in BBG in reciprocal space near the hole-doped vHs at $\mu = \mu_0 + \lambda_I$, at T_c given in Fig. 3 in the main text, for $\lambda_I = 0, 1, 2, 3, 4, 5$ meV, from left to right. (b) Real space screened potential for $\lambda_I = 0$ meV (red), $\lambda_I = 1$ meV (blue), $\lambda_I = 2$ meV (green), $\lambda_I = 3$ meV (cyan), $\lambda_I = 4$ meV (magenta), $\lambda_I = 5$ meV (orange). (c) Inset of (b) near the minimum of the screened potential.

λ_I (meV)	r_{min} (nm)	$V_{scr}(r_{min})$ (eV)
0.0	12.1985	-0.199664
1.0	12.2834	-0.210588
2.0	12.3683	-0.220475
3.0	12.4532	-0.232751
4.0	12.5381	-0.251644
5.0	12.5381	-0.251644

Table I. Relation between Ising SOC strength, λ_I , the minimum of the screened potential and its position in real space near the hole-doped vHs of BBG at the critical temperatures shown in Fig. 3 in the main text.

As for the results, the splitting induces two superconducting peaks as a function of Fermi energy, as shown in Fig. S5 and seen in the experiments of Ref. [4]. When the Fermi energy is placed at the $\mu_0 + \lambda_I$ vHs, the vHs at $\mu_0 - \lambda_I$ is nearly or completely unpopulated, depending on the value of λ_I , so the non-superconducting state is nearly or completely polarized to a half-metal. In this case, superconductivity is notably enhanced. In contrast, when μ is at the $\mu_0 - \lambda_I$ vHs, the flavours at the $\mu_0 + \lambda_I$ vHs have large Fermi surfaces. This situation leads to smaller critical temperatures than without spin-orbit, for any reasonable value of λ_I , which implies that the large Fermi surfaces away from μ have a detrimental effect on superconductivity.

Finally, it is also possible to consider a superconducting wavefunction involving only Cooper pairs $|K^+ \uparrow, K^- \downarrow\rangle$, which interact with themselves via spin-valley flips. In this case, we find the same critical temperatures as shown in Fig. 3 in the main text for the vHs at $\mu_0 + \lambda_I$.

IV. SUPERCONDUCTIVITY IN BBG WITH ELECTRON DOPING

As can be seen in Fig. 2 in the main text, the critical temperature peaks close to the vHs in the DOS, which suggests that superconductivity could also exist near the vHs of the conduction band. In order to confirm this we compute the critical temperature around this vHs with the same procedure. The results can be found in Fig. S6. We find a $T_c \approx 15$ mK near the vHs of the conduction band in BBG. After including the short-range interaction, the critical temperature increases to $T_c \approx 25$ mK. The OP is qualitatively similar to the one with hole-doping.

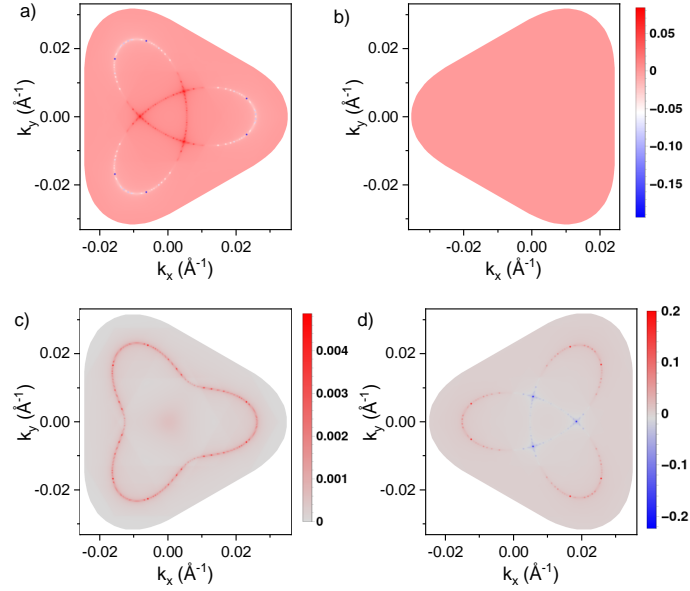


Figure S4. Order parameter of hole doped BBG with Ising SOC $\lambda_I = 1$ meV, at $\mu = \mu_0 + \lambda_I$, in (a) in valley K^+ and (b) in valley K^- , (c,d) same as (a,b), at $\mu = \mu_0 - \lambda_I$, where μ_0 is the Fermi energy at which the vHs appears in absence of Ising SOC.

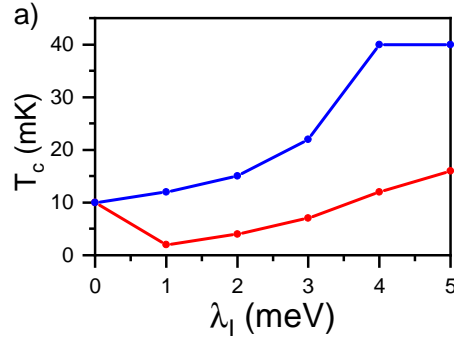


Figure S5. Critical temperature in hole-doped BBG with Ising spin-orbit coupling, at both vHs. Blue data correspond to the vHs at $\mu = \mu_0 + \lambda_I$, while red data correspond to the vHs at $\mu = \mu_0 - \lambda_I$, where μ_0 is the Fermi energy at which the vHs appears in absence of Ising SOC.

V. DIAGRAMS

Figure S7 shows the diagrams involved in superconductivity. We assume that Cooper pairs are formed between electrons in different valleys. Diagram (a) represents the long-range interaction, mediated by the screened Coulomb potential. After scattering, each carrier remains in its original valley. The kernel Γ^+ corresponds to this diagram, while Γ^- corresponds to a diagram with K^+ and K^- exchanged. The global wavefunction is $|\Psi\rangle \propto |\mathbf{K}^+, \uparrow; \mathbf{K}^-, \downarrow\rangle \pm |\mathbf{K}^+, \downarrow; \mathbf{K}^-, \uparrow\rangle$. The ‘+’ combination corresponds to valley-singlet, spin-triplet pairing, while the ‘-’ combination results in valley-triplet, spin-singlet pairing. In the absence of short-range interactions, these two pairings are degenerate. Diagram (b) represents the short-range interaction of the model, which is mediated by a repulsive, momentum-independent Hubbard $U = 3$ eV. After scattering, the carriers exchange valley. This interaction can break the degeneracy between the two pairings mentioned above.

Focusing on the superconducting OP in Fig. 4 in the main text, one might wonder why the OP in each panel lives in the Fermi surface of only one valley, even though one panel corresponds to $\hat{\Delta}^+$ and the other to $\hat{\Delta}^-$, each of which stems from diagrams involving both valleys. The reason for this is the application of time reversal symmetry (TRS). The two matrix elements involved in diagram (a) can be expressed in terms of quantities in valley K^+ only, after applying TRS. An analogous argument applies to the panel that plots the $\hat{\Delta}^-$ part of the eigenvector. This time, we use TRS to express all quantities in the valley K^- . The short-range interaction is a small perturbation that does not

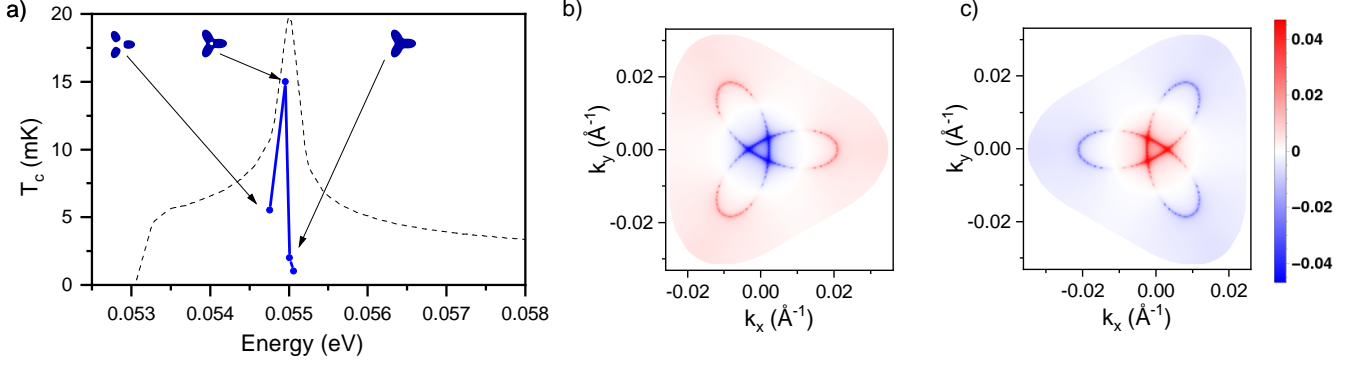


Figure S6. (a) Critical temperature (blue) and DOS (a.u., dashed black) versus Fermi energy in electron-doped BBG with a field-induced gap of 98 meV. The insets show the shape of the Fermi surface. (b) Order parameter at the energy for which $T_c = 15$ mK, in valley \mathbf{K}^+ and (c) valley \mathbf{K}^- . Again a sign change between valleys is visible, thus pointing to the valley-singlet, spin-triplet nature of the superconducting state in BBG. The maximum T_c is found near the vHs, with $n_e \approx 0.385 \cdot 10^{12} \text{ cm}^{-2}$.

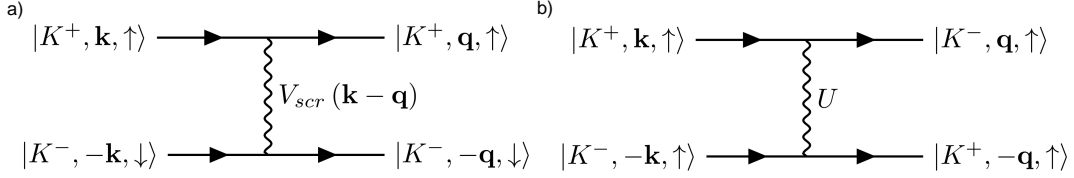


Figure S7. Diagrams of the (a) long-range interaction mediated by the screened Coulomb potential V_{scr} , which does not change the valley of the incoming states. (b) Short-range interaction mediated by the momentum independent Hubbard U , which makes the incoming states exchange valley.

change this picture.

VI. THE GAP EQUATION

We construct the gap equation following similar steps as if we were working with the BCS theory but instead of setting an electron-phonon coupling as mediator of the interaction between the pairs, we assume that the electron-electron interaction alone leads to pairing, which essentially is the Kohn-Luttinger methodology in [28]. This purely electronic interaction is the screened long-range Coulomb potential that a carrier feels within the system, which ultimately we consider to be the glue of the pairs. As there are many carriers playing a role in electronic interactions we account for the screening of the potential via the Random Phase Approximation (RPA).

Now we proceed to derive Eqs. (6, 7) in the main text. We start from the gap equation (4), which includes two terms, one for the screened long-range Coulomb potential V_{scr} and another for the short-range Hubbard repulsion U ,

$$\tilde{\Delta}^{+,i,j}(\mathbf{k}) = -\frac{K_B T}{\Omega} \sum_{\mathbf{q}, \omega} \sum_{i', j'} \left[V_{scr}(\mathbf{k} - \mathbf{q}) G_{K^+}^{i, i'}(\mathbf{q}, i\omega) G_{K^-}^{j, j'}(-\mathbf{q}, -i\omega) \tilde{\Delta}^{+,i', j'}(\mathbf{q}) + U G_{K^-}^{i, i'}(\mathbf{q}, i\omega) G_{K^+}^{j, j'}(-\mathbf{q}, -i\omega) \tilde{\Delta}^{-,j', i'}(-\mathbf{q}) \right]. \quad (\text{S5})$$

We can work separately with the long-range and short-range terms and then simply develop the equations. We begin with the kernel of the long-range interaction and substitute the electrons' Green's functions by their definitions,

$$G_{\mathbf{K}\xi}^{i, i'}(\mathbf{k}, \pm i\omega) = \sum_n \frac{\Psi_{\xi, n}^i(\mathbf{k}) \Psi_{\xi, n}^{i', *}(\mathbf{k})}{i\omega \mp \epsilon_{\mathbf{K}\xi, n}(\mathbf{k})}, \text{ leading to,}$$

$$\begin{aligned}
\tilde{\Delta}_{n,m}^{+,i,j}(\mathbf{k}) &= -\frac{K_B T}{\Omega} \sum_{\mathbf{q}, \omega} \sum_{i', j'} V_{scr}(\mathbf{k} - \mathbf{q}) G_{K^+}^{i, i'}(\mathbf{q}, i\omega) G_{K^-}^{j, j'}(-\mathbf{q}, -i\omega) \tilde{\Delta}^{+, i', j'}(\mathbf{q}), \\
&= -\frac{K_B T}{\Omega} \sum_{\mathbf{q}, \omega} \sum_{i', j'} V_{scr}(\mathbf{k} - \mathbf{q}) \frac{\Psi_{K^+, n}^i(\mathbf{q}) \Psi_{K^+, n}^{i', *}(\mathbf{q}) \Psi_{K^-, m}^j(-\mathbf{q}) \Psi_{K^-, m}^{j', *}(-\mathbf{q})}{i\omega - \epsilon_{K^+, n}(\mathbf{q}) i\omega + \epsilon_{K^-, m}(-\mathbf{q})} \tilde{\Delta}^{+, i', j'}(\mathbf{q}), \\
&= -\frac{K_B T}{\Omega} \sum_{\mathbf{q}} V_{scr}(\mathbf{k} - \mathbf{q}) \Psi_{K^+, n}^i(\mathbf{q}) \Psi_{K^-, m}^j(-\mathbf{q}) \sum_{\omega} \frac{1}{i\omega - \epsilon_{K^+, n}(\mathbf{q})} \frac{1}{i\omega + \epsilon_{K^-, m}(-\mathbf{q})} \sum_{i', j'} \Psi_{K^+, n}^{i', *}(\mathbf{q}) \Psi_{K^-, m}^{j', *}(-\mathbf{q}) \tilde{\Delta}^{+, i', j'}(\mathbf{q}), \\
&= -\frac{K_B T}{\Omega} \sum_{\mathbf{q}} V_{scr}(\mathbf{k} - \mathbf{q}) \Psi_n^i(\mathbf{q}) \Psi_m^{j, *}(\mathbf{q}) \sum_{\omega} \frac{1}{i\omega - \epsilon_n(\mathbf{q})} \frac{1}{i\omega + \epsilon_m(\mathbf{q})} \sum_{i', j'} \Psi_n^{i', *}(\mathbf{q}) \Psi_m^{j'}(\mathbf{q}) \tilde{\Delta}^{+, i', j'}(\mathbf{q}), \\
&= -\frac{1}{\Omega} \sum_{\mathbf{q}} V_{scr}(\mathbf{k} - \mathbf{q}) \Psi_n^i(\mathbf{q}) \Psi_m^{j, *}(\mathbf{q}) \frac{f(-\epsilon_m(\mathbf{q})) - f(\epsilon_n(\mathbf{q}))}{\epsilon_n(\mathbf{q}) + \epsilon_m(\mathbf{q})} \tilde{\Delta}_{n,m}^+(\mathbf{q}),
\end{aligned} \tag{S6}$$

where in the last step we have performed a Matsubara sum using $\sum_{i\omega} \frac{1}{i\omega - \epsilon_1} \frac{1}{i\omega + \epsilon_2} = \frac{1}{K_B T} \frac{1}{\epsilon_1 + \epsilon_2} [f(-\epsilon_2) - f(\epsilon_1)]$, thus,

$$\sum_{i, j} \Psi_n^{i, *}(\mathbf{k}) \Psi_m^j(\mathbf{k}) \tilde{\Delta}_{n,m}^{+, i, j}(\mathbf{k}) = -\frac{1}{\Omega} \sum_{\mathbf{q}} V_{scr}(\mathbf{k} - \mathbf{q}) \frac{f(-\epsilon_m(\mathbf{q})) - f(\epsilon_n(\mathbf{q}))}{\epsilon_n(\mathbf{q}) + \epsilon_m(\mathbf{q})} \sum_{i, j} \Psi_n^{i, *}(\mathbf{k}) \Psi_m^j(\mathbf{k}) \Psi_n^i(\mathbf{q}) \Psi_m^{j, *}(\mathbf{q}) \tilde{\Delta}_{n,m}^+(\mathbf{q}). \tag{S7}$$

Here we introduce the new quantity $\tilde{\tilde{\Delta}}^+(\mathbf{p}) = \tilde{\Delta}^+(\mathbf{p}) \sqrt{\frac{f(-\epsilon_m(\mathbf{p})) - f(\epsilon_n(\mathbf{p}))}{\epsilon_n(\mathbf{p}) + \epsilon_m(\mathbf{p})}}$ for the kernel to be hermitian, so after the substitution,

$$\tilde{\tilde{\Delta}}_{n,m}^+(\mathbf{k}) = -\frac{1}{\Omega} \sum_{\mathbf{q}} V_{scr}(\mathbf{k} - \mathbf{q}) \sqrt{\frac{f(-\epsilon_m(\mathbf{k})) - f(\epsilon_n(\mathbf{k}))}{\epsilon_n(\mathbf{k}) + \epsilon_m(\mathbf{k})}} \sqrt{\frac{f(-\epsilon_m(\mathbf{q})) - f(\epsilon_n(\mathbf{q}))}{\epsilon_n(\mathbf{q}) + \epsilon_m(\mathbf{q})}} \sum_{i, j} \Psi_n^{i, *}(\mathbf{k}) \Psi_m^j(\mathbf{k}) \Psi_n^i(\mathbf{q}) \Psi_m^{j, *}(\mathbf{q}) \tilde{\Delta}_{n,m}^+(\mathbf{q}). \tag{S8}$$

Now, following the same procedure we continue with the kernel of the short-range interaction.

$$\begin{aligned}
\tilde{\Delta}_{n,m}^{+,i,j}(\mathbf{k}) &= -U \frac{K_B T}{\Omega} \sum_{\mathbf{q}, \omega} \sum_{i', j'} G_{K^-}^{i, i'}(\mathbf{q}, i\omega) G_{K^+}^{j, j'}(-\mathbf{q}, -i\omega) \tilde{\Delta}^{-, j', i'}(-\mathbf{q}), \\
&= -U \frac{K_B T}{\Omega} \sum_{\mathbf{q}, \omega} \sum_{i', j'} \frac{\Psi_{K^-, n}^i(\mathbf{q}) \Psi_{K^-, n}^{i', *}(\mathbf{q}) \Psi_{K^+, m}^j(-\mathbf{q}) \Psi_{K^+, m}^{j', *}(-\mathbf{q})}{i\omega - \epsilon_{K^-, n}(\mathbf{q}) i\omega + \epsilon_{K^+, m}(-\mathbf{q})} \tilde{\Delta}^{-, j', i'}(-\mathbf{q}), \\
&= -U \frac{K_B T}{\Omega} \sum_{\mathbf{q}} \Psi_{K^-, n}^i(\mathbf{q}) \Psi_{K^+, m}^j(-\mathbf{q}) \sum_{\omega} \frac{1}{i\omega - \epsilon_{K^-, n}(\mathbf{q})} \frac{1}{i\omega + \epsilon_{K^+, m}(-\mathbf{q})} \sum_{i', j'} \Psi_{K^-, n}^{i', *}(\mathbf{q}) \Psi_{K^+, m}^{j', *}(-\mathbf{q}) \tilde{\Delta}^{-, j', i'}(-\mathbf{q}), \\
&= -U \frac{K_B T}{\Omega} \sum_{\mathbf{q}} \Psi_n^{i, *}(-\mathbf{q}) \Psi_m^j(-\mathbf{q}) \sum_{\omega} \frac{1}{i\omega - \epsilon_n(-\mathbf{q})} \frac{1}{i\omega + \epsilon_m(-\mathbf{q})} \sum_{i', j'} \Psi_n^{i'}(-\mathbf{q}) \Psi_m^{j', *}(-\mathbf{q}) \tilde{\Delta}^{-, j', i'}(-\mathbf{q}), \\
&= -U \frac{K_B T}{\Omega} \sum_{\mathbf{q}} \Psi_n^{i, *}(\mathbf{q}) \Psi_m^j(\mathbf{q}) \sum_{\omega} \frac{1}{i\omega - \epsilon_n(\mathbf{q})} \frac{1}{i\omega + \epsilon_m(\mathbf{q})} \sum_{i', j'} \Psi_n^{i'}(\mathbf{q}) \Psi_m^{j', *}(\mathbf{q}) \tilde{\Delta}^{-, j', i'}(\mathbf{q}), \\
&= -U \frac{K_B T}{\Omega} \sum_{\mathbf{q}} \Psi_n^{i, *}(\mathbf{q}) \Psi_m^j(\mathbf{q}) \sum_{\omega} \frac{1}{i\omega - \epsilon_n(\mathbf{q})} \frac{1}{i\omega + \epsilon_m(\mathbf{q})} \sum_{i', j'} \Psi_m^{i', *}(\mathbf{q}) \Psi_n^{j'}(\mathbf{q}) \tilde{\Delta}^{-, i', j'}(\mathbf{q}), \\
&= -U \frac{1}{\Omega} \sum_{\mathbf{q}} \Psi_n^{i, *}(\mathbf{q}) \Psi_m^j(\mathbf{q}) \frac{f(-\epsilon_m(\mathbf{q})) - f(\epsilon_n(\mathbf{q}))}{\epsilon_n(\mathbf{q}) + \epsilon_m(\mathbf{q})} \tilde{\Delta}_{n,m}^-(\mathbf{q}),
\end{aligned} \tag{S9}$$

thus,

$$\sum_{i, j} \Psi_n^{i, *}(\mathbf{k}) \Psi_m^j(\mathbf{k}) \tilde{\Delta}_{n,m}^{+, i, j}(\mathbf{k}) = -U \frac{1}{\Omega} \sum_{\mathbf{q}} \frac{f(-\epsilon_m(\mathbf{q})) - f(\epsilon_n(\mathbf{q}))}{\epsilon_n(\mathbf{q}) + \epsilon_m(\mathbf{q})} \sum_{i, j} \Psi_n^{i, *}(\mathbf{k}) \Psi_m^j(\mathbf{k}) \Psi_n^{i, *}(\mathbf{q}) \Psi_m^j(\mathbf{q}) \tilde{\Delta}_{n,m}^-(\mathbf{q}), \tag{S10}$$

and we arrive at,

$$\tilde{\Delta}_{n,m}^+(\mathbf{k}) = -U \frac{1}{\Omega} \sum_{\mathbf{q}} \sqrt{\frac{f(-\epsilon_m(\mathbf{k})) - f(\epsilon_n(\mathbf{k}))}{\epsilon_n(\mathbf{k}) + \epsilon_m(\mathbf{k})}} \sqrt{\frac{f(-\epsilon_m(\mathbf{q})) - f(\epsilon_n(\mathbf{q}))}{\epsilon_n(\mathbf{q}) + \epsilon_m(\mathbf{q})}} \sum_{i,j} \Psi_n^{i,*}(\mathbf{k}) \Psi_m^j(\mathbf{k}) \Psi_n^{i,*}(\mathbf{q}) \Psi_m^j(\mathbf{q}) \tilde{\Delta}_{n,m}^-(\mathbf{q}). \quad (\text{S11})$$

Combining Eqs. (S8, S11) along with time reversal symmetry gives Eqs. (6, 7) in the main text.

VII. CRITICAL TEMPERATURE DEPENDENCE ON ELECTRIC FIELD.

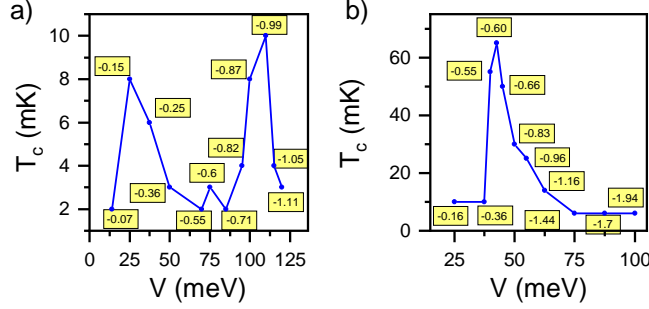


Figure S8. Electric field dependence of the critical temperature near the vHs of hole-doped (a) BBG and (b) RTG. Yellow boxes label the electronic density at which the critical temperature has been computed for each case, in units of 10^{12} cm^{-2}

Figure S8 indicates the critical temperatures of BBG and RTG, as a function of the external electric field. T_c peaks at a certain field, and tends to diminish when the field changes. These results are in qualitative agreement with the experimental findings in Refs. [1, 9].

VIII. THE ROLE OF THE HUBBARD U.

We conclude with a tentative discussion on the effects of the value of U , which is the least well determined parameter in our model. Realistic values $U \sim 2 - 4 \text{ eV}$. [59, 60]. We recall here that the screened long-range Coulomb interaction leads to a degeneracy between valley-triplet, spin-singlet and valley-singlet, spin-triplet pairings. The short-range Hubbard-like interaction can break this degeneracy, selecting a preferred pairing symmetry. For the value used in this work, $U = 3 \text{ eV}$, the short-range interaction can be seen as a small perturbation. In BBG and RTG, an infinitesimally small value of U is enough to break the aforementioned degeneracy. To first order in perturbation theory, the change in the kernel eigenvalue due to the short-range interaction is:

$$\delta\epsilon = - \sum_{\mathbf{k}, \mathbf{k}'} \tilde{\Delta}_{\mathbf{k}} \tilde{U}(\mathbf{k}, \mathbf{k}') \tilde{\Delta}_{\mathbf{k}'}, \quad (\text{S12})$$

where $\tilde{\Delta}_{\mathbf{k}}$ and $\tilde{\Delta}_{\mathbf{k}'}$ are the order parameters in valley K^+ and K^- , in the absence of the short-range interaction. From this follows the common wisdom that a repulsive, i.e. positive, U , favours valley-singlet pairing, in which the OP changes sign between valleys, so that $\delta\epsilon > 0$, resulting in an enhanced critical temperature. However, Eq. S12 is valid only for single pocket superconductors, while in BBG and RTG each valley shows at least two pockets, which makes the situation more complex, as pockets with a certain sign in one valley can interact strongly with others with the opposite sign in the other valley, even if the global state is valley-triplet, spin-singlet. Still, both BBG and RTG have valley-singlet, spin-triplet pairing for any finite value of U , which is the usual result with repulsive short-range interactions, as mentioned above.

It is illustrative to note that in the limit of large U , the short-range interaction is not a perturbation anymore, but rather becomes the leading interaction and overshadows the long-range Coulomb potential. When short-range interactions are dominant, the most energetically favorable solution is the one in which each valley has a constant sign, and there is a change of sign between valleys. Thus, for large values of U the order parameter loses the sign changes within each valley. This phenomenon occurs in both materials, although in the bilayer the intravalley signs only disappear completely at $U \gtrsim 25 \text{ eV}$.

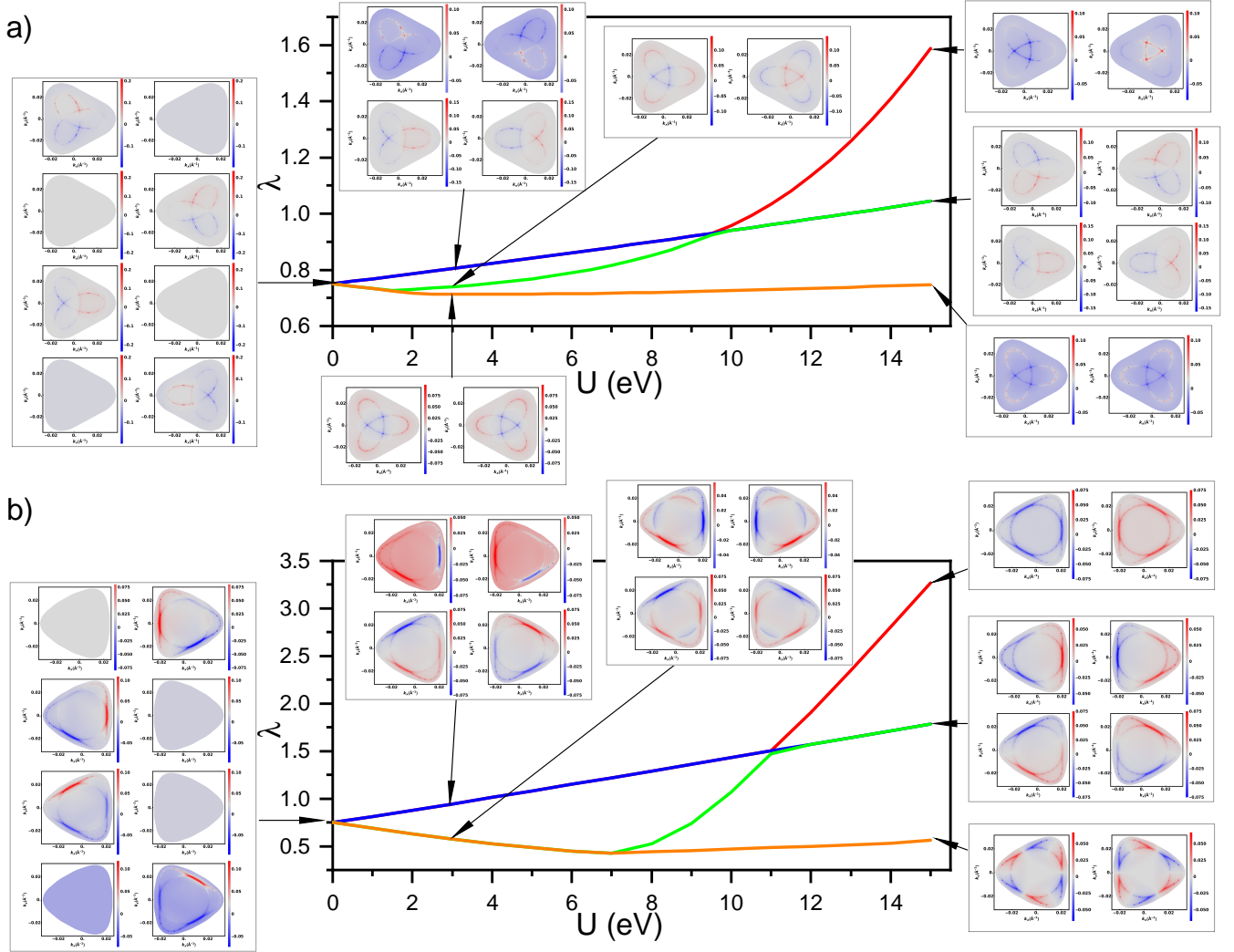


Figure S9. Symmetry of the OP, as a function of the short-range interaction strength, U , for the four largest eigenvalues near the hole-doped vHs of (a) BBG at $T = 10$ mK and (b) RTG at $T = 85$ mK. These plots are meant to illustrate the form of the order parameter as a function of U , but note that the eigenvalues $\lambda < 1$ imply that the superconducting state has not been reached here, and details change once it is, e.g. the degeneracy and associated C_3 -symmetry breaking of the largest eigenvalue of BBG at $U = 3$ eV disappears.

IX. CRITICAL TEMPERATURE STARTING FROM A HALF METAL STATE.

Figure S10 shows the critical temperature as a function of Fermi energy in both materials, when the non-superconducting state is a half metal. The calculation is equivalent to the one in Fig. 2 in the main text, but the factor of $N_f = 4$ in the susceptibility is substituted by $N_f = 2$. The situation is qualitatively similar to the one with Ising SOC. However, the complete disappearance of two flavours leads to a more severe change in the susceptibility than the energy split induced by Ising SOC. It is an approximation which gives a rough idea of what happens for very large values of λ_I . The critical temperature we find here for BBG is 80 mK, while starting from the full metal it is 10 mK, and in the experiment, 26 mK [1]. For RTG. the critical temperatures starting from a half metal or a full metal state are 110 mK and 65 mK, respectively, while the experiment reports 105 mK [9].

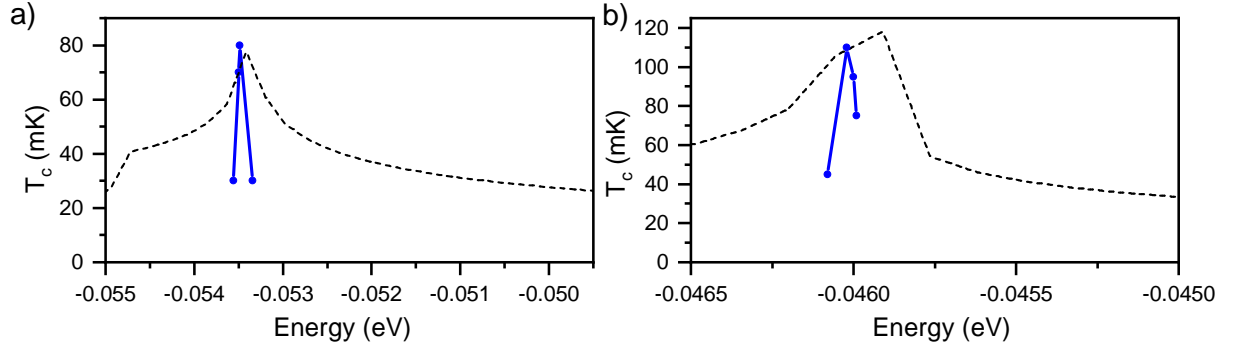


Figure S10. Superconducting critical temperature starting from a half metal non-superconducting state (solid blue) and DOS (a.u. dashed black) versus Fermi energy in (a) BGG with hole doping and a gap of 98 meV; near the vHs we observe a $T_c \approx 80$ mK, and in (b) RTG with hole doping and a gap of 74 meV; near the vHs we observe a $T_c \approx 110$ mK.